Development and experimental characterization of a robotic butterfly with a mass shifter mechanism

Haifeng Huang, Wei He [*], Ze Chen, Tao Niu, Qiang Fu

School of Intelligence Science and Technology, University of Science and Technology Beijing, Beijing 100083, China
Institute of Artificial Intelligence, University of Science and Technology Beijing, Beijing 100083, China

ARTICLE INFO

ABSTRACT

The development of biomimetic aerial robots has emerged as a new solution for studying the flight mechanisms of flying creatures. This study designs a biomimetic robotic butterfly steered via a mass shift mechanism named USTButterfly-II and investigates its flight characteristics using an optical tracking facility. First, a planar four-bar linkage was used to drive the flapping of the designed butterfly-like artificial wings. Next, an innovative tailless steering control method was proposed based on a mass shift mechanism. Finally, the wing kinematics and motion trajectory of the USTButterfly-II were measured using a multi-camera motion capture system, and some difficult-to-measure flapping aerodynamic parameters, such as the instantaneous net lift and thrust coefficients, were determined. These findings present a novel experimental framework that not only provides effective data support for the design and improvement of the robotic butterfly but also benefits the study of biological butterfly flight mechanisms.

1. Introduction

In contrast to fixed-wing and rotary-wing aircraft, insects and birds use unsteady aerodynamics-enhancing mechanisms to achieve efficient, stable, and maneuverable flight [1]. Among these flapping flyers, the specific flight morphology and behavior of butterflies distinguish their aerodynamic mechanism from others that have been studied for many years [2]. Previous studies have shown that butterflies in flight use various leading-edge vortices and flapping-wing flight mechanisms to increase aerodynamic forces [3–7]. However, the flight of butterflies remains poorly understood, particularly in terms of quantitative analysis. Taking advantage of recent advances in microelectromechanical systems technology, research on flapping-wing aerial robots has surged, providing a new method for studying the flight mechanisms of flying creatures [8–14].

Current and conventional methods for studying butterfly flight mechanisms include vivo observation and computational fluid dynamics (CFD) simulation. A visual flow field is used to investigate the unsteady aerodynamic mechanism of butterflies in free flight, but it only describes the presence of vortexes and does not yield quantitative results [2]. The authors in [15] use a motion capture system to record the free flight of the Monarch butterfly, but only the characteristics of climbing flight are studied. Because of the complexity and variability of the butterfly flight trajectory, obtaining sufficient flight characteristic parameters in vivo observation experiments is typically difficult. Using computers to simulate the flying state of butterflies is less expensive,

but it is difficult to restore their true flapping flight posture. C. L. Roy et al. conducted CFD simulation analysis on the Morpho butterflies in various ecological environments and obtained vortex field distribution and lift–drag ratio parameters [2]. However, only the aerodynamic characteristics of the gliding state are investigated, with no consideration given to the effect of wing flapping. Researchers have recently begun using biomimetic platforms to study biological mechanisms, with notable research results including Bat Bot [16], KUBeetle [17,18], and DelFly Nimble [19]. There have been few findings on the use of robotic butterflies to study butterfly flight mechanisms. Using a biomimetic platform to study butterflies' flight mechanisms can effectively avoid the problems of poor repeatability of vivo observations and poor accuracy of computational simulations, but it introduces challenges in the design and control of the robotic butterfly. Festo created the eMotionButterfly, a two-servo-driven robotic butterfly. It has a 50 cm wingspan weighing 32 g and flaps between 1 and 2 Hz [20]. The eMotionButterfly flapping frequency is much lower than that of biological butterflies, and the researchers did not conduct any additional experimental studies on its flight characteristics.

In a previous study, we developed a wire-driven robotic butterfly named USTButterfly-S with a wingspan of 50 cm that can be steered by asymmetrically adjusting the areas of the two wings [21]. However, in this study, we developed the USTButterfly-II, a biomimetic robotic butterfly capable of free controlled flight, and used the Optitrack motion capture system to record its flight and analyze its flight characteristics. Unlike the servo-driven method in [20–22], the wings of
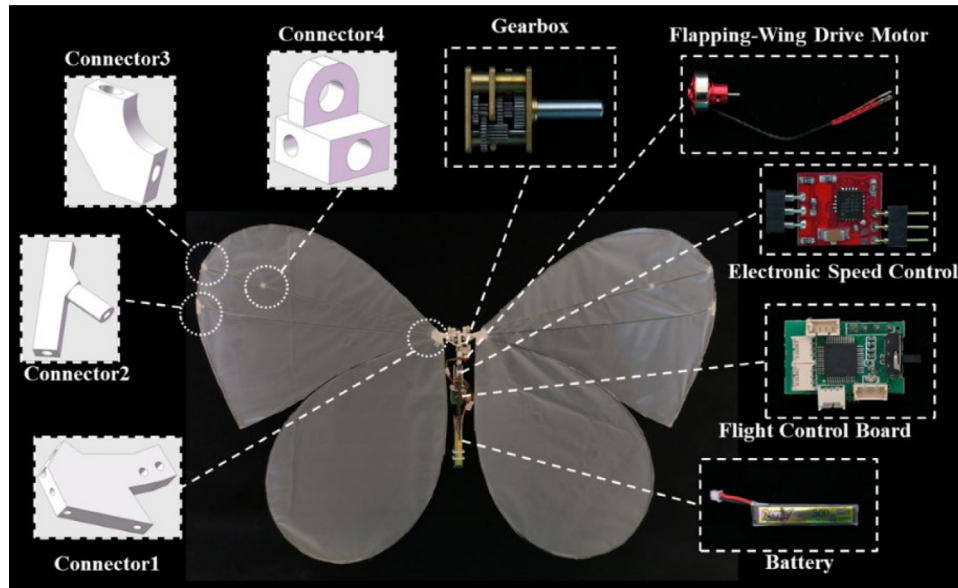

Fig. 1. Configurations of our self-designed robotic butterfly named USTButterfly-II.

USTButterfly-II are driven to flap periodically by a motor and a planar four-bar linkage. The flapping amplitude of USTButterfly-II exceeds 80°, and the flapping frequency was 5 Hz, making it more similar to the wing flapping characteristics of biological butterflies than the previous robotic butterfly. In terms of the wing design, the wing skeleton was made of carbon rods, and the wing membrane was made of chlorinated polyethylene film. This fabrication method allows artificial wings to be lighter in weight and have more elastic deformation properties. For the steering control of USTButterfly-II, a mass shifter mechanism was creatively designed. Steering was accomplished by adjusting the position of the mass shifter mechanism. The mass shifter mechanism, which has a simple structure and low failure rate, allowed the flapping and steering control to operate independently.

The wing kinematics and motion trajectory of the USTButterfly-II were measured and analyzed for several sequential flaps using 14 high-speed motion-tracking cameras. Various flight parameters such as real-time flight trajectory, three-axis attitude angles, wing flapping angle, and lift and thrust coefficients, were calculated based on the three-dimensional spatial coordinates of the reflection markers attached to USTButterfly-II to analyze the flight characteristics of the robotic butterfly and compare them with biological butterflies. The experimental results indicated that the robotic butterfly was similar to biological butterflies in some aspects, which aids in the quantitative and qualitative analysis of butterfly flight mechanisms. The following are the main contributions of this study:

(1) To investigate the flight mechanism of biological butterflies, a biomimetic robotic butterfly capable of free controlled flight was designed.

(2) To propose a novel steering control mechanism for the tailless robotic butterfly. The steering control of the robotic butterfly was achieved by rotating the mass shifter mechanism on the fuselage.

(3) To propose a novel experimental framework for the experimental characterization of the robotic butterfly, which not only provides valuable data support for the design and improvement of the robotic butterfly but also contributes to the investigation of biological butterfly flight mechanisms.

This research is divided into three sections. The development of the robotic butterfly is described in Section 2. Section 3 describes the motion capture experiment, the method for calculating flight characteristics, and the experimental results. Section 4 presents the study's findings.

2. Development of the robotic butterfly

This section presents the system composition and design method of USTButterfly-II from three perspectives: system overview, design of the flapping-wing drive subsystem, and design of the mass shifter mechanism.

2.1. System overview

As a common butterfly species, researchers have extensively studied swallowtail butterflies based on their morphological and flight characteristics. These findings were used as a reference for the design of the robotic butterfly and the comparative analysis with biology. A robotic butterfly capable of free controlled flight was designed by imitating the wing shape and flapping characteristics of swallowtail butterflies, as shown in Fig. 1. The robotic butterfly has two pairs of wings with skeletons made of carbon fiber rods of varying diameters, which include carbon fiber rods with diameters of 1.3 mm, 1.5 mm and 1 mm, used for the edges, main rods and ribs of the forewings and hindwings, respectively. The carbon rods were formed into skeleton shapes by inserting 3D printed connectors. The flapping drive mechanism was made up of a brushless motor, a micro gearbox, and a planar four-bar linkage. A mass shifter mechanism was designed to alert the robot's center of mass, which consists of the flight control board, electronic speed control, steering servo, battery, and skeleton. The self-designed flight control board was 16.3 mm*23.2 mm in size and 2.8 g in weight. An 8.8 g lithium battery was used as the robot's power source. The prototype weighed 54 g in total, and its weight decomposition is shown in Fig. 2.

2.2. Design of the flapping-wing drive subsystem

The drive subsystem's design is linked to wing kinematics and is critical to the development of the robotic butterfly. Butterfly wings, unlike those of other insects such as flies and bees, do not rotate during flapping strokes [23]. Therefore, the drive subsystem only needs to implement the wings' translational flap. As shown in Fig. 3, the drive subsystem adopts a planar four-bar linkage mechanism, with two rockers that cause the wings to flap periodically. To reduce the weight, the gears were made of polyacetal resin, and the rockers, linkages, and frame parts were made of nylon PA11. Except for the metal gearbox, all components were made using 3D printing.
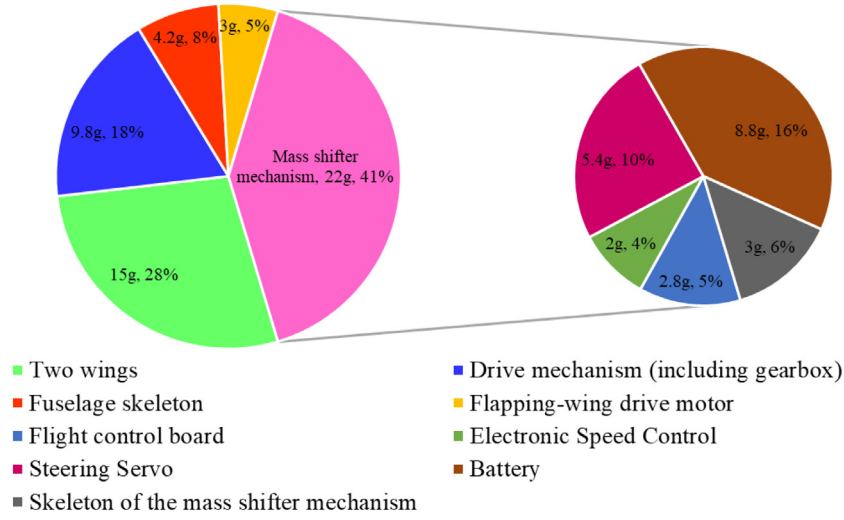
Fig. 2. Weight decomposition of USTButterfly-II. The mass shifter mechanism, including the flight control board, electronic speed control, steering servo, battery, and skeleton, weighs 22 g, accounting for 41% of the entire robot (55 g).
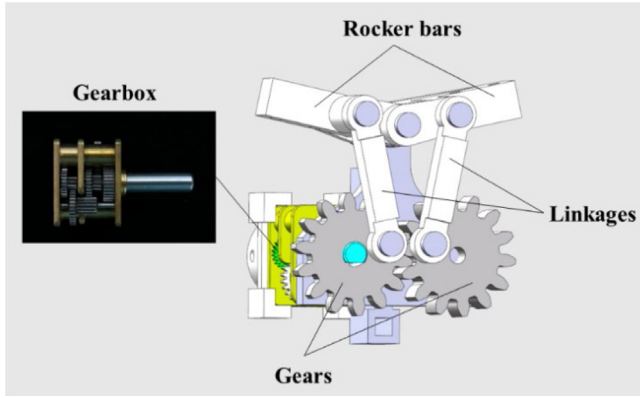

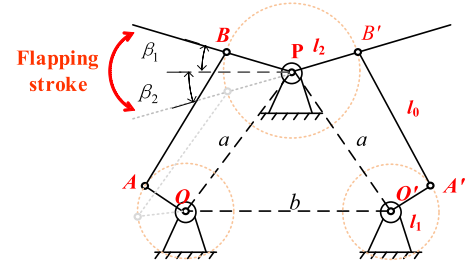**Fig. 3.** Flapping-wing driving mechanism of USTButterfly-II.

Fig. 4. Schematic of the four-bar linkage with double cranks and double rockers.

Fig. 4 shows the schematic of the four-bar linkage with double cranks and double rockers, where P is the rocker anchor point, O and O′ are the centers of the gears, OA and O′A′ are the length of the cranks l_1, AB and A′B′ are the length of the linkages l_0, and PB and PB′ are the length of the rockers l_2. Due to the symmetry of the structure, $\Delta POO'$ is an isosceles triangle (PO=PO′ = a, OO′ = b), with OO′ parallel to the horizontal plane. Define the rack mounting angle as $\alpha = arccos(b/2a)$ and the wing flapping angle as β, which is positive when the wing is above the horizontal plane. When the linkage AB and the crank OA are collinear, the flapping angle β reaches its maximum and minimum values, which are expressed as follows:

$$\beta_{max} = arccos(l_2^2 + a^2 - (l_0 + l_1)^2)/(2al_2) - \alpha \tag{1}$$

$$\beta_{min} = arccos(l_2^2 + a^2 - (l_0 - l_1)^2)/(2al_2) - \alpha \tag{2}$$

According to vivo observation data [15], the flapping frequency of Monarch butterflies in flight ranges from 9 Hz to 11 Hz, and the flapping amplitude ranges from 191° to 291°. Previous research has shown that enlarged robotic butterflies can provide sufficient lift with reduced wing flapping frequency and amplitude [20,21]. Given the limitation of motor output power, the robotic butterfly was designed to flap its wings up and down at an equal amplitude of 42°, i.e., $\beta_{max} = 42°$ and $\beta_{min} = -42°$. The specific structural parameters were set as follows: $a = 16.8$ mm, $b = 13$ mm, $l_0 = 15.65$ mm, $l_1 = 4$ mm, and $l_2 = 6$ mm.

2.3. Design of the mass shifter mechanism

Unlike bird-like flapping-wing robots that use a tail to control their direction, the tailless structure of the robotic butterfly makes steering control difficult [24,25]. Some biological creatures, such as lizards, improve their maneuverability through the intelligent use of mass and inertia. Similarly, we proposed an innovative steering control mechanism for a robotic butterfly. As shown in Fig. 5, the designed mass shifter mechanism includes the steering servo, electronic speed control, battery, flight control board, and skeleton. The robotic butterfly's center of mass is altered by controlling the steering servo, which rotates the entire mechanism. Due to the rotation of the mass shifter mechanism, the center of mass of the robotic butterfly was deflected, resulting in a rolling motion.

Fig. 6(a) shows the yaw torque-producing mechanism when the roll angle of USTButterfly-II is not zero. F_L in the figure represent the lift, and the superscripts R and L represent the right and left wings, respectively. The arc-shaped shading represents the flapping stroke. For simplicity, the net propulsive force generated by a flapping cycle (one upstroke and one downstroke) was assumed to equal the force on the stroke's center plane. By resolving the lift into its horizontal and vertical components, the vertical force was used to overcome gravity, and the horizontal force pointing to the left wing produced a yaw moment. As shown by the force resolution, the magnitude (direction) of the roll angle influenced the magnitude (direction) of the horizontal force. Therefore, the robotic butterfly's steering can be monitored by controlling the angle of rotation and direction of the steering servo. Actual flight experiments validated the effectiveness of the steering control mechanism, and Fig. 6(b) is an example of an indoor right-turn flight.
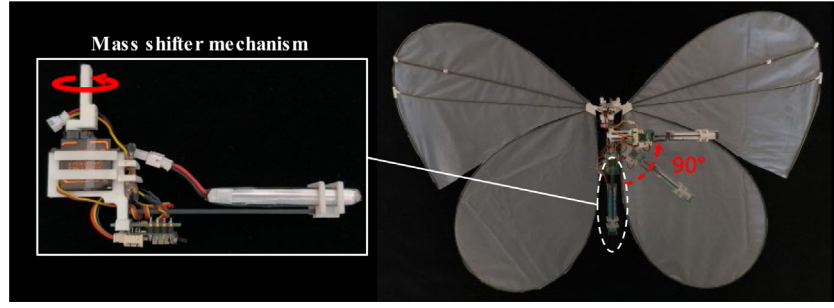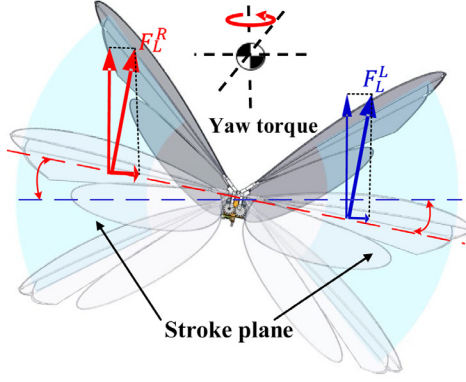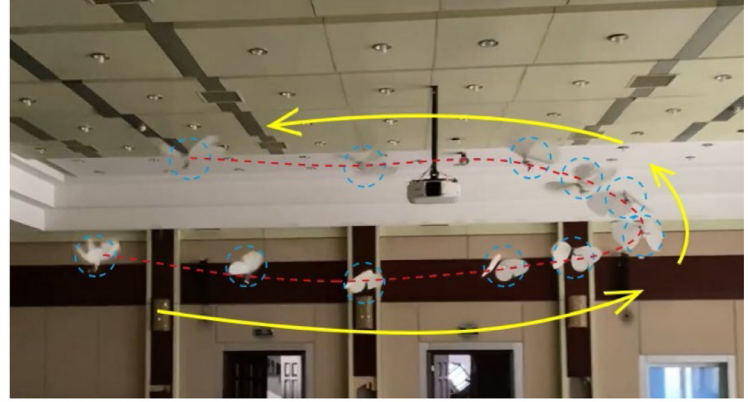
Fig. 5. Rotation of the mass shifter mechanism when USTButterfly-II turns right.
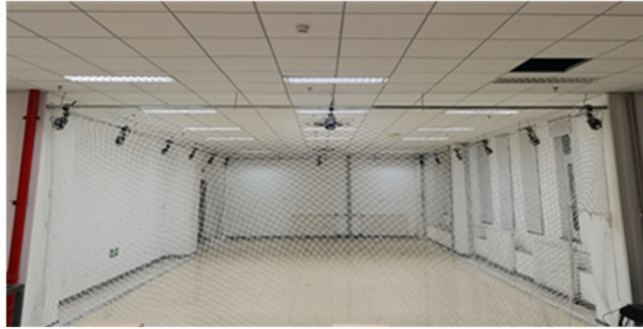

(a) Yaw torque-producing mechanism.

(b) Demonstration of an indoor right-turn flight experiment.

Fig. 6. Demonstrations of the yaw torque-producing mechanism and the actual flight experiment.

(a) Experimental site.

(b) Camera placement.

Fig. 7. Optitrack motion capture system used to record the flight of USTButterfly-II.

3. Experimental characterization of the robotic butterfly

An optical tracking facility was used to record the free flight of USTButterfly-II to quantify the flight characteristics of the robotic butterfly. This section contains a detailed description of the experimental methodology and results.

3.1. Experimental setup

The experiments were conducted using the Optitrack motion capture system, which includes 14 cameras that capture an area of about 85 square meters. The experimental site and the top view of the camera arrangement are shown in Fig. 7(a) and Fig. 7(b), respectively.

For subsequent experiments, the combination of reflective balls and stickers was chosen based on the weight of the markers and the reflective effect. The paste locations of the reflective markers are shown in Fig. 8, and the properties of each marker are listed in Table 1. Markers #1–4 and #9–12 are the corresponding markers on the back and abdomen sides of the wings, and they are located on the left forewing, right forewing, left hindwing, and right hindwing, respectively. Attaching reflective stickers to the wingtips improves the system's capture rate on the one hand and records the deformation of the wing on the other hand. At the same time, the reflective marks are overlapped and attached to the corresponding position to prevent them from being lost when the wings are flapping. Markers #5–8 are affixed to the fuselage marker points.

3.2. Data postprocessing

In this subsection, some typical flight parameters were defined and calculated to describe the flight characteristics of robotic butterflies quantitatively. First, the 3-axis attitude and flapping angles of the
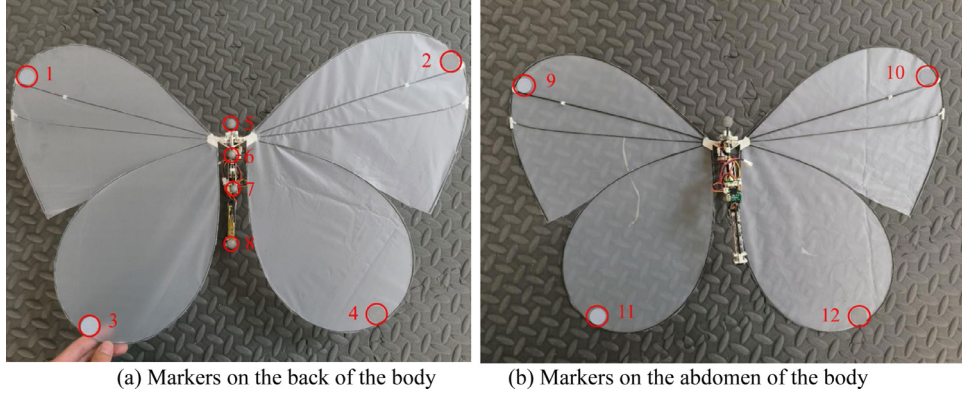
(a) Markers on the back of the body
(b) Markers on the abdomen of the body

Fig. 8. Marker locations in red circles.

Table 1
Properties of the markers.

Marker #	Diameter dimensions, cm	Type
1	2	Round stickers
2	2	Round stickers
3	2	Round stickers
4	2	Round stickers
5	1.5	Sphere
6	1	Hemispheroid
7	1	Hemispheroid
8	1.5	Sphere
9	2	Round stickers
10	2	Round stickers
11	2	Round stickers
12	2	Round stickers

Fig. 9. Establishment of the body coordinate system and the ground coordinate system.

forewings and hindwings were calculated. Furthermore, the angle of attack, lift, thrust, and their respective coefficients were calculated. Finally, the ascent angle was defined and calculated to gauge the climbing efficiency, and the propulsion ratio and flight speed were defined and calculated to gauge the propulsion efficiency.

As shown in Fig. 9, the body coordinate system $O_b X_b Y_b Z_b$ was established with the origin O_b located at the robot's center of mass. The X_b axis is perpendicular to the symmetric plane of the body and points to the right, Y_b axis is perpendicular to the X_b axis and points upwards. Z_b is located in the symmetric plane of the body and forms a right-hand rectangular coordinate system with X_b and Y_b. The motion capture system can provide the spatial coordinates of the reflective markers in the ground coordinate system $OXYZ$, as shown in the lower left corner of Fig. 9.

3.2.1. Calculation of the attitude angles

Before calculating the attitude angle, the real-time coordinates of each axis of the body coordinate system in the ground coordinate system should be determined. As shown in Fig. 10, the body coordinate system was calculated using three markers.

The three markers, A, B, and C, are all located in the plane $Y_b O_b Z_b$. The intersection angle between $-\overrightarrow{Z_b}$ and $\overrightarrow{BA}$ is $\alpha = 10°$ and $\angle ABC = 25°$. Because the X_b is perpendicular to the plane ABC, the X_b axis vector is given as $\overrightarrow{X_b} = \overrightarrow{BA} \times \overrightarrow{BC}$. Assuming that the length of $\overrightarrow{Z_b}$ is 1, $\overrightarrow{Z_b} = (x_z, y_z, z_z)$ can be determined by the following equations:

$$
\begin{cases}
\left| \overrightarrow{Z_b} \right| = 1 \\
\overrightarrow{Z_b} \cdot \overrightarrow{X_b} = 0 \\
\cos(\alpha) = \dfrac{-\overrightarrow{Z_b} \cdot \overrightarrow{BA}}{\left| \overrightarrow{BA} \right|} \\
\arccos \left(\dfrac{-\overrightarrow{Z_b} \cdot \overrightarrow{BC}}{\left| \overrightarrow{BC} \right|} \right) < \angle ABC.
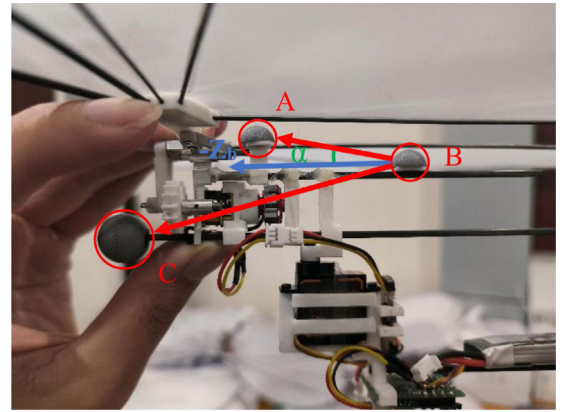\end{cases}
\tag{3}
$$

Fig. 10. Reference markers used for calculating the body coordinate system.

Also, since the Y_b axis is perpendicular to the plane $X_b O_b Z_b$ pointing upward, the vector of the Y_b axis is given as $\overrightarrow{Y_b} = \overrightarrow{Z_b} \times \overrightarrow{X_b}$. Furthermore, the pitch angle θ can be determined as follows:

$$
\theta = \begin{cases}
\arccos \dfrac{\overrightarrow{Z_b} \cdot (0,1,0)}{\left| \overrightarrow{Z_b} \right|} - \dfrac{\pi}{2}, & (z_z \geq 0) \\
-\arccos \dfrac{\overrightarrow{Z_b} \cdot (0,1,0)}{\left| \overrightarrow{Z_b} \right|} - \dfrac{\pi}{2}, & (z_z < 0 \wedge y_z \geq 0) \\
-\arccos \dfrac{\overrightarrow{Z_b} \cdot (0,1,0)}{\left| \overrightarrow{Z_b} \right|} + \dfrac{3\pi}{4}, & (z_z < 0 \wedge y_z < 0)
\end{cases}
\tag{4}
$$
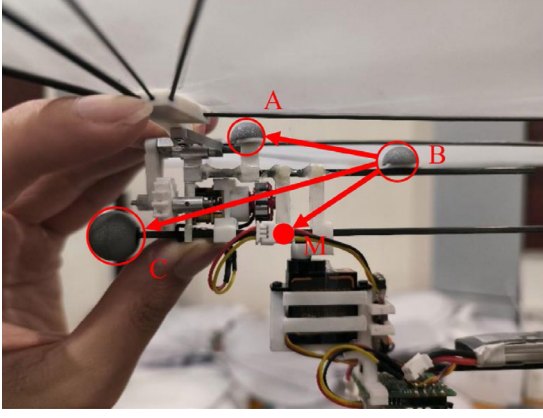
Fig. 11. Reference markers used for calculating the coordinates of the center of mass.

Fig. 12. Reference markers used for calculating the flapping angles of the wings.

Assuming the projection $\overrightarrow{Z_b}$ on the ground plane XOZ is $\overrightarrow{Z_{b,xoz}} = (x_z, 0, z_z)$, then the yaw angle φ can be determined as follows:

$$\varphi = \begin{cases} \arccos \dfrac{\overrightarrow{Z_{b,xoz}} \cdot (0,0,1)}{\left|\overrightarrow{Z_{b,xoz}}\right|}, (x_z \geq 0) \\ -\arccos \dfrac{\overrightarrow{Z_{b,xoz}} \cdot (0,0,1)}{\left|\overrightarrow{Z_{b,xoz}}\right|}, (x_z < 0) \end{cases} \tag{5}$$

Define $\overrightarrow{Y_b} = (x_y, y_y, z_y)$ and $\overrightarrow{VER_{Z_b}} = (0,1,0) \times \overrightarrow{Z_b}$, then the roll angle γ can be determined as follows:

$$\gamma = \begin{cases} \arccos \dfrac{\overrightarrow{VER_{Z_b}} \cdot \overrightarrow{Y_b}}{\left|\overrightarrow{VER_{Z_b}}\right|\left|\overrightarrow{Y_b}\right|} - \dfrac{\pi}{2}, (y_y \geq 0) \\ -\arccos \dfrac{\overrightarrow{VER_{Z_b}} \cdot \overrightarrow{Y_b}}{\left|\overrightarrow{VER_{Z_b}}\right|\left|\overrightarrow{Y_b}\right|} - \dfrac{\pi}{2}, (y_y < 0 \wedge x_y > 0) \\ -\arccos \dfrac{\overrightarrow{VER_{Z_b}} \cdot \overrightarrow{Y_b}}{\left|\overrightarrow{VER_{Z_b}}\right|\left|\overrightarrow{Y_b}\right|} + \dfrac{3\pi}{4}, (y_y < 0 \wedge x_y \leq 0) \end{cases} \tag{6}$$

Next, the coordinates of the center of mass were calculated, and the markers used are shown in Fig. 11, where M is the center of mass, and the four points A, B, C, and M are coplanar with $\angle ABM = 42°$, $\angle CBM = 18°$, and $\left|\overrightarrow{BM}\right| = 0.039$ m.

Then, the vector $\overrightarrow{BM}$ can be determined using the following equations:

$$\begin{cases} \left|\overrightarrow{BM}\right| = 0.039 \\ \overrightarrow{BM} \cdot \overrightarrow{X_b} = 0 \\ \cos(\angle ABM) = \dfrac{\overrightarrow{BM} \cdot \overrightarrow{BA}}{\left|\overrightarrow{BM}\right|\left|\overrightarrow{BA}\right|} \\ \arccos(\dfrac{\overrightarrow{BM} \cdot \overrightarrow{BC}}{\left|\overrightarrow{BM}\right|\left|\overrightarrow{BC}\right|}) < \angle ABM \end{cases} \tag{7}$$

3.2.2. Calculation of the flapping angles of the wings

The reference markers used to calculate the flapping angles of the wings are shown in Fig. 12, with point A located on the wing root rotation axis, and W_{FL}, W_{FR}, W_{RL}, and W_{RR} are the makers on the left forewing, right forewing, left hindwing, and right hindwing, respectively.

Let ϕ_{FL}, ϕ_{FR}, ϕ_{RL} and ϕ_{RR} be the flapping angles of the left forewing, right forewing, left hindwing, and right hindwing, respectively. Since the flapping angles of all four wings were calculated in the same way, the flapping angle of the left forewing was used as
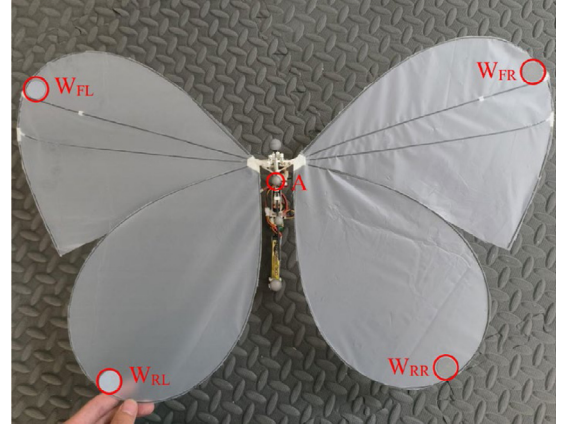
an example. Defining the projection $\overrightarrow{AW_{FL}}$ on the $X_b O_b Y_b$ plane as $\overrightarrow{AW_{FL,XOY}}$ results in the following equation:

$$\overrightarrow{AW_{FL,XOY}} = \overrightarrow{AW_{FL}} - \frac{(\overrightarrow{AW_{FL}} \cdot \overrightarrow{Z_b}) \cdot \overrightarrow{Z_b}}{\left|\overrightarrow{Z_b}\right|^2} \tag{8}$$

$$\phi_{FL} = \frac{\pi}{2} - \arccos \frac{\overrightarrow{AW_{FL,XOY}} \cdot \overrightarrow{Y_b}}{\left|\overrightarrow{AW_{FL,XOY}}\right|\left|\overrightarrow{Y_b}\right|} \tag{9}$$

3.2.3. Calculation of the lift and thrust coefficients

The following assumptions were made to calculate the lift and thrust in this study: first, the lift and thrust of the left and right wings were assumed to be equal; second, the lift direction was defined in the same direction as the Y_b axis, and the thrust direction was defined in the opposite direction to the Z_b axis. Under these assumptions, the calculation of lift and thrust requires solving the 3-axis acceleration of the center of mass in the body coordinate system $O_b X_b Y_b Z_b$. Thus, the rotation transformation from the ground coordinate system to the body coordinate system must first be conducted. Define the 3-axis acceleration of the center of mass in the ground and the body coordinate systems as $a_{Mb} = \begin{bmatrix} a_{Mbx} & a_{Mby} & a_{Mbz} \end{bmatrix}^T$ and $a_{Mb} = \begin{bmatrix} a_{Mbx} & a_{Mby} & a_{Mbz} \end{bmatrix}^T$, respectively. The equation can be expressed as follows: $a_{Mb} = Ra_M = R_z \times R_y \times R_x \times a_M$, where

$$R_x = \begin{bmatrix} 1 & 0 & 0 \\ 0 & \cos\theta & \sin\theta \\ 0 & -\sin\theta & \cos\theta \end{bmatrix}, R_y = \begin{bmatrix} \cos\varphi & 0 & \sin\varphi \\ 0 & 1 & 0 \\ -\sin\varphi & 0 & \cos\varphi \end{bmatrix}, \text{ and }$$

$$R_z = \begin{bmatrix} \cos\gamma & -\sin\gamma & 0 \\ \sin\gamma & \cos\gamma & 0 \\ 0 & 0 & 1 \end{bmatrix}. \tag{10}$$

Let the coordinate of the center of mass in the ground coordinate system be $M_t = \begin{bmatrix} x_{M,t} & y_{M,t} & z_{M,t} \end{bmatrix}^T$, the 3-axis velocity be $v_t = \begin{bmatrix} v_{x,t} & v_{y,t} & v_{z,t} \end{bmatrix}^T$, and the 3-axis acceleration is $a_{M,t} = \begin{bmatrix} a_{Mx,t} & a_{My,t} & a_{Mz,t} \end{bmatrix}^T$. The sampling frequency of the motion capture system was 240 Hz. The equation is given as follows:

$$v_t = (M_{t+1} - M_t)f \tag{11}$$

$$a_{M,t} = (v_{t+1} - v_t)f \tag{12}$$

Let the acceleration of the center of mass in the body coordinate system be $a_{Mb,t} = \begin{bmatrix} a_{Mbx,t} & a_{Mby,t} & a_{Mbz,t} \end{bmatrix}^T$, then $a_{Mb,t} = R_t a_{M,t}$. The total mass of the robotic butterfly with the reflective markers is measured as $m = 0.0596$ kg, and the gravitational acceleration is $g = 9.8$ m/s^2. The gravity in the ground coordinate system is $G =$
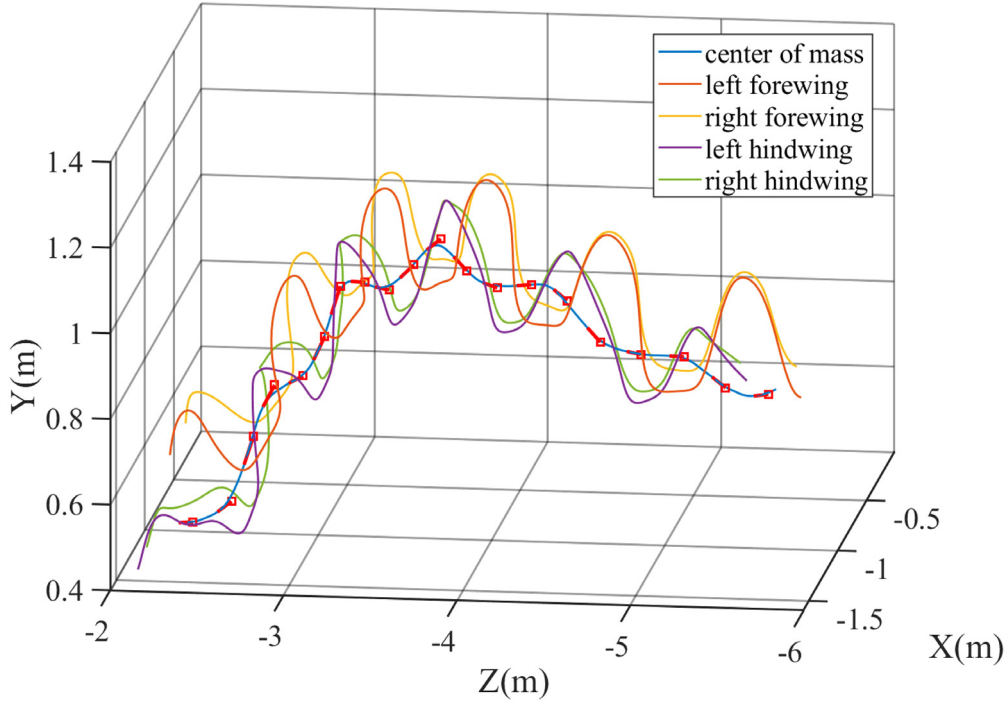
Fig. 13. Spatial and temporal variations in the center of mass and the markers on the wings.

$\begin{bmatrix} 0 & mg & 0 \end{bmatrix}^T$, and the gravity in the body coordinate system is $G_{b,t} = \begin{bmatrix} x_{Gb,t} & y_{Gb,t} & z_{Gb,t} \end{bmatrix}^T = R_t G$. Let the lift and thrust of a single wing be $F_{L,t}$ and $F_{T,t}$, and the total lift and thrust be $F_{Ls,t}$ and $F_{Ts,t}$, respectively. The equation can be expressed as follows:

$$\begin{cases} F_{Ls,t} = a_{Mby,t}m - y_{Gb,t} \\ F_{L,t} = \dfrac{F_{Ls,t}}{2} \\ F_{Ts,t} = -a_{Mbz,t}m \\ F_{T,t} = \dfrac{F_{Ts,t}}{2} \end{cases} \tag{13}$$

Furthermore, the instantaneous lift and thrust coefficients can be determined by the equation as follows:

$$\begin{cases} C_{L,t} = \dfrac{2F_{L,t}}{\rho V_t^2 S} \\ C_{T,t} = \dfrac{2F_{T,t}}{\rho V_t^2 S} \end{cases} \tag{14}$$

where $C_{L,t}$ is the lift coefficient of a single wing, $C_{T,t}$ is the thrust coefficient of a single wing, ρ is the air density, S is the area of a single wing, and $V_t = \|v_t\|_2$ is the body's speed relative to air.

3.2.4. Calculation of the angle of attack

Define the angle of attack at the time t as α_t, the angle formed by the intersecting $-\overrightarrow{Z_b}$ and the projection v_t on the $Y_b O_b Z_b$ plane. Define the velocity vector in the body coordinate system as $v_{b,t} = \begin{bmatrix} x_{vb,t} & y_{vb,t} & z_{vb,t} \end{bmatrix}^T$ thus $v_{b,t} = R_t v_t$ and $v_{yoz,t} = \begin{bmatrix} 0 & y_{vb,t} & z_{vb,t} \end{bmatrix}^T$. Furthermore, the angle of attack can be determined by the equation as follows:

$$\alpha_t = \begin{cases} \arccos \dfrac{v_{yoz,t} \cdot [0,0,-1]}{|v_{yoz,t}|}, & y_{vb,t} <= 0 \\ -\arccos \dfrac{v_{yoz,t} \cdot [0,0,-1]}{|v_{yoz,t}|}, & y_{vb,t} > 0 \end{cases} \tag{15}$$

3.2.5. Definition of flight motion metrics

In addition to the conventional parameters listed above, three new metrics to quantify the flight performance of the robotic butterfly were

devised: flight-averaged speed, advance ratio, and ascent angle. The flight-averaged speed V is the average speed of the entire flight phase. Let the spatial coordinates of the center of mass at the time t_1 and t_2 be $M_{t1} = \begin{bmatrix} x_{M,t1} & y_{M,t1} & z_{M,t1} \end{bmatrix}^T$ and $M_{t2} = \begin{bmatrix} x_{M,t2} & y_{M,t2} & z_{M,t2} \end{bmatrix}^T$, respectively. Thus, V can be expressed by the following equation:

$$V = \frac{\|M_{t2} - M_{t1}\|_2}{t_2 - t_1} \tag{16}$$

The ascent angle γ_{ascent} defined to gauge the climbing efficiency of the entire flight phase and can be expressed by the following equation:

$$\begin{aligned} \gamma_{ascent} &= \arctan \left(\frac{d_{ver}}{d_{hor}} \right) \\ &= \arctan \left(\frac{y_{M,t2} - y_{M,t1}}{\sqrt{(x_{M,t2} - x_{M,t1})^2 + (z_{M,t2} - z_{M,t1})^2}} \right) \end{aligned} \tag{17}$$

The advance ratio $R_{advance}$ is defined to gauge the propulsive efficiency of the entire flight phase and can be expressed with the following equation:

$$R_{advance} = \frac{V}{f_{flap}} \tag{18}$$

where f_{flap} is the flapping frequency referring to the reciprocal of the time difference between the end of two consecutive upstrokes.

3.3. Results

The motion capture system data includes the position and velocity of each of the 12 markers, and the software's cubic polynomial interpolation function was used to supplement the missing markers in the experiment. This subsection uses measurements from a flight lasting six flapping cycles as an example.

Fig. 13 shows the spatial and temporal variations in the center of mass and the markers on the wings, with the red arrow indicating the speed vector of the current position. The entire flight process lasts for approximately six flapping cycles. The first three flapping cycles at 4.4 Hz correspond to the climbing stage with a 21.8° ascent angle. The subsequent three flapping cycles at 4.8 Hz correspond to the descending
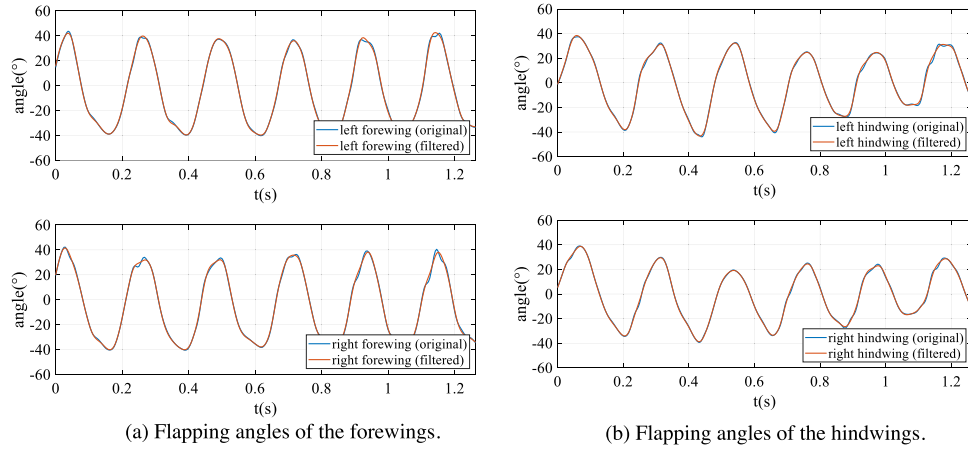
(a) Flapping angles of the forewings.

(b) Flapping angles of the hindwings.

Fig. 14. Variations in the flapping angles of the wings.
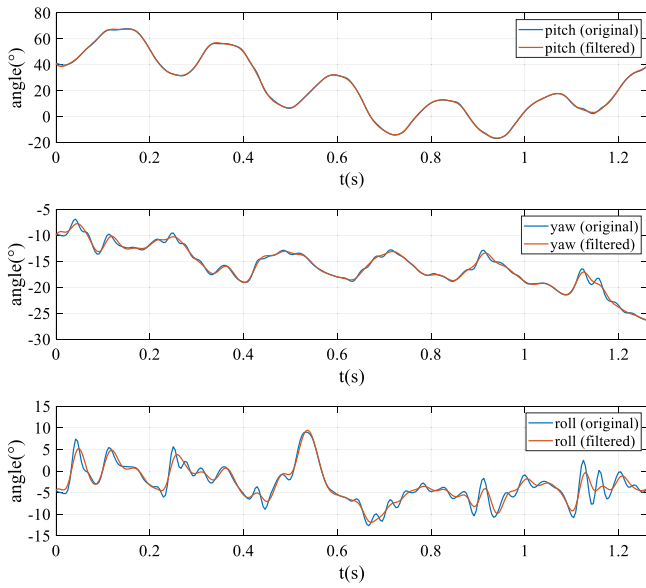

Fig. 15. Variations in the 3-axis attitude angles.
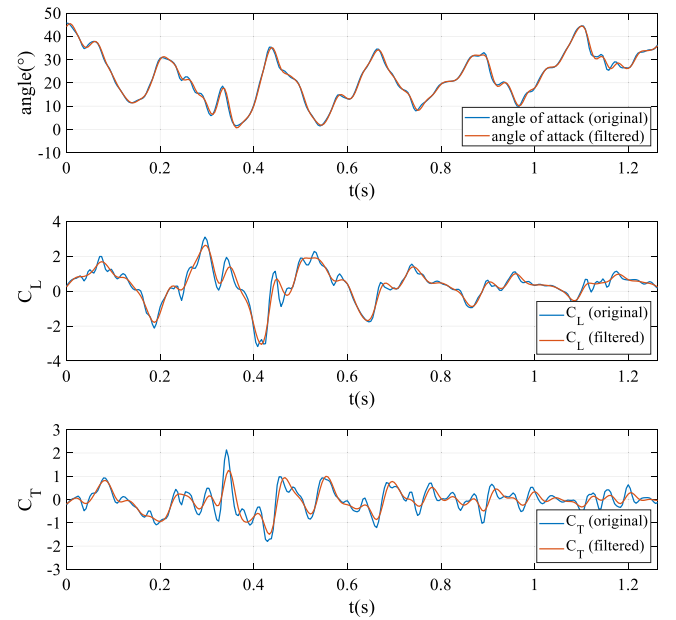

Fig. 16. Variations in the angle of attack, lift and thrust coefficients.

stage with an ascent angle of −13.9°. This finding implies that the lift is not always positively correlated with the flapping frequency. The downstroke of the forewing corresponds to the upstroke of the body undulation, indicating that the wing's downstroke is the primary stage of lift generation.

The variations in the flapping angles are shown in Fig. 14. The flapping angles can be seen to fluctuate sinusoidally with a peak value of about 40°, and the flapping angles of the left and right wings are nearly identical. The flapping frequency of the hindwing follows that of the forewing with a time lag of about 0.05 s, owing to the difference in deformation between the forewing and hindwing. The flapping amplitude of the hindwing changes continuously with the change in the attitude angles during the entire flight process because the hindwing is designed to be more flexible. Furthermore, the flapping amplitude is greater in the climbing phase than in the descending phase, which is closely related to the aerodynamic force acting on the forewing. These findings imply that the hindwing functions as a stabilizer similar to the tail of a bird-like flapping-wing robot, and the robotic butterfly can be controlled by adjusting the flexibility of the hindwing.

The variations in the attitude angles are shown in Fig. 15. The pitch angle also fluctuates in a sinusoidal pattern that roughly synchronizes with the body's undulation. Furthermore, the pitch angle increases

during the downstroke and decreases during the upstroke, indicating that it is essentially opposite to the forewing flapping angle. During the climbing phase, the pitch angle fluctuates around 40°, and the fuselage clearly points upward. Also, during the descending stage, the pitch angle fluctuates around 0°, indicating that the fuselage is at the basic level, which is consistent with the actual flight trajectory. Note that the pitch angle explicitly increases in the last flapping cycle because the robotic butterfly transitions to a climbing flight after descending. Due to the asymmetry of the fuselage, without applying heading control, the yaw and roll angles fluctuate in a small range and do not exhibit any obvious regularity.

In this experiment, the robotic butterfly's flight speed and flapping frequency do not change significantly. Therefore, the focus was entirely on analyzing the relationship between the lift and thrust with the angle of attack. Fig. 16 shows the variations in the angle of attack, lift, and thrust coefficients. The angle of attack ranges from 0° to 50°. Despite the lag, the angle of attack strongly correlates with the lift coefficient. A possible explanation for the lag is due to the unsteady flapping-wing aerodynamic properties. The lift's peak and trough appear at the beginning of the wingbeat's downstroke and upstroke, respectively. The Lift variation was discovered to be closely related to the flapping

Table 2
Flight parameters of USTButterfly-II and Monarch butterflies in climbing flight.

Parameter	USTButterfly-II	Monarch
Wingspan (cm)	50	5.3
Flapping frequency (Hz)	4.4	9.6
Flapping amplitude (°)	80	128
Wing loading (N m^{-2})	3.8	2.8
Flight-averaged speed V (m s^{-1})	2.35	1.77
Advanced ratio $R_{advance}$ (m)	0.53	0.18

frequency. During the climbing stage, the lift force decreases with a decrease in flapping frequency and gradually increases with an increase in flapping frequency during the descending stage. In comparison to lift, no obvious fluctuation law of thrust was discovered.

Table 2 lists the climbing flight parameters of USTButterfly-II and Monarch butterflies [15]. In contrast, the flapping frequency and flapping amplitude of USTButterfly-II are significantly lower than those of the Monarch butterfly. However, the wing load, flight speed, and advance ratio of USTButterfly-II are significantly greater than those of the Monarch butterfly, possibly due to the robotic butterfly's larger size.

4. Conclusion

In this study, a biomimetic robotic butterfly capable of free controlled flight named USTButterfly-II was designed. An innovative mass shifter mechanism was designed to realize the robotic butterfly's tailless steering control, which was validated by an actual flight experiment. A novel experimental framework was presented by combining the optical tracking facility and the robotic butterfly to enhance our understanding of the design of the robotic butterfly and the flight mechanism of biological butterflies. The quantitative flight parameters of the robotic butterfly were successfully obtained through experiments which revealed that the robotic butterfly has some flight characteristics similar to biological butterflies.

Declaration of competing interest

The authors declare that they have no known competing financial interests or personal relationships that could have appeared to influence the work reported in this paper.

Acknowledgments

Appendix A. Supplementary data

Supplementary material related to this article can be found online at https://doi.org/10.1016/j.birob.2022.100076.

References

[1] R.B. Srygley, A.L.R. Thomas, Unconventional lift-generating mechanisms in free-flying butterflies, Nature 420 (6916) (2002) 660–664.

[2] C. Le Roy, D. Amadori, S. Charberet, et al., Adaptive evolution of flight in morpho butterflies, Science 374 (6571) (2021) 1158–1162.

[3] M.H. Dickinson, F.O. Lehmann, S.P. Sane, Wing rotation and the aerodynamic basis of insect flight, Science 284 (5422) (1999) 1954–1960.

[4] S.P. Sane, M.H. Dickinson, The control of flight force by a flapping wing: lift and drag production, J. Exp. Biol. 204 (15) (2001) 2607–2626.

[5] W. He, Z. Li, C.L.P. Chen, A survey of human-centered intelligent robots: issues and challenges, IEEE/CAA J. Autom. Sin. 4 (4) (2017) 602–609.

[6] W. He, X. Mu, L. Zhang, et al., Modeling and trajectory tracking control for flapping-wing micro aerial vehicles, IEEE/CAA J. Autom. Sin. 8 (1) (2020) 148–156.

[7] J.M. Birch, M.H. Dickinson, Spanwise flow and the attachment of the leading-edge vortex on insect wings, Nature 412 (6848) (2001) 729–733.

[8] D. Floreano, R.J. Wood, Science, technology and the future of small autonomous drones, Nature 521 (7553) (2015) 460–466.

[9] J. Luo, D. Huang, Y. Li, et al., Trajectory online adaption based on human motion prediction for teleoperation, IEEE Trans. Autom. Sci. Eng. 19 (4) (2021) 3184–3191.

[10] X. Bai, Y. Wang, S. Wang, et al., Modeling and analysis of an underwater biomimetic vehicle-manipulator system, Sci. China Inf. Sci. 65 (3) (2021) 134201.

[11] J. Yu, X. Li, L. Pang, et al., Design and attitude control of a novel robotic jellyfish capable of 3D motion, Sci. China Inf. Sci. 62 (9) (2019) 194201:1-194201:3.

[12] F.Y. Hsiao, L.J. Yang, S.H. Lin, et al., Autopilots for ultra lightweight robotic birds: Automatic altitude control and system integration of a sub-10 g weight flapping-wing micro air vehicle, IEEE Control Syst. Mag. 32 (5) (2012) 35–48.

[13] L.J. Yang, B. Esakki, U. Chandrasekhar, et al., Practical flapping mechanisms for 20 cm-span micro air vehicles, Int. J. Micro Air Vehicles 7 (2) (2015) 181–202.

[14] Z. Tu, F. Fei, J. Zhang, et al., An at-scale tailless flapping-wing hummingbird robot. I. Design, optimization, and experimental validation, IEEE Trans. Robot. 36 (5) (2020) 1511–1525.

[15] C. Kang, J. Cranford, M.K. Sridhar, et al., Experimental characterization of a butterfly in climbing flight, AIAA J. 56 (1) (2018) 15–24.

[16] A. Ramezani, S.J. Chung, S. Hutchinson, A biomimetic robotic platform to study flight specializations of bats, Science Robotics 2 (3) (2017) eaal2505.

[17] H.V. Phan, S. Aurecianus, T.K.L. Au, et al., Towards the long-endurance flight of an insect-inspired, tailless, two-winged, flapping-wing flying robot, IEEE Robot. Autom. Lett. 5 (4) (2020) 5059–5066.

[18] H.V. Phan, H.C. Park, Mechanisms of collision recovery in flying beetles and flapping-wing robots, Science 370 (6521) (2020) 1214–1219.

[19] M. Karásek, F.T. Muijres, C. De Wagter, et al., A tailless aerial robotic flapper reveals that flies use torque coupling in rapid banked turns, Science 361 (6407) (2018) 1089–1094.

[20] H.V. Phan, H.C. Park, Insect-inspired, tailless, hover-capable flapping-wing robots: Recent progress, challenges, and future directions, Prog. Aerosp. Sci. 111 (2019) 100573.

[21] H. Huang, W. He, Y. Zou, et al., System design and control of a butterfly-inspired flapping-wing aerial robot based on wire-driven steering (in Chinese), Control Theory Appl. 39 (7) (2022) 1203–1210.

[22] H. Huang, W. He, J. Wang, et al., An all servo-driven bird-like flapping-wing aerial robot capable of autonomous flight, IEEE/ASME Trans. Mechatronics (2022) http://dx.doi.org/10.1109/TMECH.2022.3182418, in press.

[23] H. Tanaka, I. Shimoyama, Forward flight of swallowtail butterfly with simple flapping motion, Bioinspiration Biomim. 5 (2) (2010) 026003.

[24] T. Lin, L. Zheng, T. Hedrick, et al., The significance of moment-of-inertia variation in flight manoeuvres of butterflies, Bioinspiration Biomim. 7 (4) (2012) 044002.

[25] J. Jayakumar, K. Senda, N. Yokoyama, Control of pitch attitude by abdomen during forward flight of two-dimensional butterfly, J. Aircr. 55 (6) (2018) 2327–2337.